Assessing the Benefits of Specific Attenuation for Quantitative Precipitation Estimation with a C-Band Radar Network

JU-YU CHEN,[a] SILKE TRÖMEL,[a,b] ALEXANDER RYZHKOV,[c] AND CLEMENS SIMMER[a]

[a] *Institute for Geosciences, Department of Meteorology, University of Bonn, Bonn, Germany*
[b] *Laboratory for Clouds and Precipitation Exploration, Geoverbund ABC/J, Bonn, Germany*
[c] *Cooperative Institute for Mesoscale Meteorological Studies, University of Oklahoma, Norman, Oklahoma*

(Manuscript received 15 December 2020, in final form 21 June 2021)

ABSTRACT: Recent advances demonstrate the benefits of radar-derived specific attenuation at horizontal polarization (A_H) for quantitative precipitation estimation (QPE) at S and X band. To date the methodology has, however, not been adapted for the widespread European C-band radars such as those installed in the network of the German Meteorological Service (DWD, Deutscher Wetterdienst). Simulations based on a large dataset of drop size distributions (DSDs) measured over Germany are performed to investigate the DSD dependencies of the attenuation parameter α_H for the A_H estimates. The normalized raindrop concentration (Nw) and the change of differential reflectivity (Z_{DR}) with reflectivity at horizontal polarization (Z_H) are used to categorize radar observations into regimes for which scan-wise optimized α_H values are derived. For heavier continental rain with $Z_H > 40$ dBZ, the A_H-based rainfall retrieval $R(A_H)$ is combined with a rainfall estimator using a substitute of specific differential phase (K^*_{DP}). We also assess the performance of retrievals based on specific attenuation at vertical polarization (A_V). Finally, the regime-adapted hybrid QPE algorithms are applied to four convective cases and one stratiform case from 2017 to 2019, and compared to DWD's operational Radar-Online-Aneichung (RADOLAN) RW rainfall product, which is based on Z_h only but adjusted to rain gauge measurements. For the convective cases, our hybrid retrievals outperform the traditional $R(Z_h)$ and pure $R(A_{H/V})$ retrievals with fixed $\alpha_{H/V}$ values when evaluated with gauge measurements and outperform RW when evaluated by disdrometer measurements. Potential improvements using ray-wise $\alpha_{H/V}$ and segment-wise applications of the ZPHI method along the radials are discussed.

KEYWORDS: Data quality control; Radars/Radar observations; Remote sensing; Precipitation

1. Introduction

Ground-based radar observations provide the core information for quantitative precipitation estimation (QPE), observation-based nowcasting, and flash flood prediction, and QPE products are further used for the evaluation of numerical models (Sun 2005; Clark et al. 1972; Zacharov and Rezacova 2010). Earlier precipitation products based on the linear reflectivity at horizontal polarization $R(Z_h)$ were highly sensitive to the variability of the raindrop size distribution (DSD) and thus lead to high uncertainties (Battan 1973). The utilization of polarimetric radar variables during the past three decades has improved QPE performance (Zrnić and Ryzhkov 1999), e.g., by utilization of differential reflectivity (Z_{DR}) characterizing the average drop size (Scarchilli et al. 1993; Zrnić et al. 2000). Since the use of Z_h and Z_{DR} requires reliable calibration, phase-based observables such as specific differential phase (K_{DP}) have been utilized more recently, also because of their lower sensitivity to DSD variations, immunity to moderate attenuation, wet radome effect, and partial beam blockage (PBB) caused by terrain or local obstacles such as buildings or trees (Ryzhkov et al. 2014; Diederich et al. 2015a,b). Hydrometeor type-specific retrievals have also been developed (Steinert et al. 2013) based on polarimetric classification algorithms (Bringi et al. 1984). The $R(K_{DP})$ is particularly suggested for heavy rain (Zrnić and Ryzhkov 1999) or situations when rain is mixed with hail (Ryzhkov et al. 2013) while its noisiness in light rain must, however, be counteracted by spatial averaging.

Lately, specific attenuation at horizontal/vertical polarization ($A_{H/V}$) emerged as a powerful information source for QPE because of its almost linear relation with the liquid water content and an even lower sensitivity to the DSD variability compared to K_{DP} (Atlas and Ulbrich 1977; Matrosov et al. 2005). Since $A_{H/V}$ also requires phase-based observations, namely, the differential phase shift (Φ_{DP}), $R(A_{H/V})$ inherits all advantages of $R(K_{DP})$ (Kurri and Huuskonen 2008; Ryzhkov et al. 2014), but is less noisy in light rain and thus comparable in spatial resolution to rainfall maps derived from $R(Z_h)$. It is recommended for area-wide composite rainfall maps (Ryzhkov et al. 2014; Diederich et al. 2015a,b). Moreover, temperature effects on the intercept parameter in $R(A_{H/V})$ relations and on the attenuation parameter $\alpha_{H/V}$ nearly cancel each other out and can be ignored (Wang et al. 2014). While the $R(A_{H/V})$ technique is frequently used for S- and X-band radars (Ryzhkov et al. 2014; Wang et al. 2019; Zhang et al. 2020; Diederich et al. 2015a,b), only few applications are known for C band because of detrimental resonance effects associated with large raindrops and hail in this wavelength range [see studies of Giangrande et al. (2014), Wang et al. (2014), and Boodoo et al. (2015) in the United States, Taiwan, and Canada, separately].

From previous studies, it indicates that the DSD sensitivity of $\alpha_{H/V}$ needs to be accounted for in the $R(A_{H/V})$ algorithms, which use the ZPHI method [the correction of measured Z_h

Denotes content that is immediately available upon publication as open access.

Corresponding author: Ju-Yu Chen, jchen@uni-bonn.de

DOI: 10.1175/JHM-D-20-0299.1

using the total constraint Φ_{DP}, see Testud et al. (2000) and Eqs. (2)–(6) in this paper] for estimating $A_{H/V}$. To this goal, the estimated change of Z_{DR} with given $Z_{H/V}$ in dBZ ($\Delta Z_{DR}/\Delta Z_{H/V}$) can be exploited. Since this so-called Z_{DR} slope is not affected by potential radar system biases of $Z_{H/V}$ and Z_{DR}, it is especially recommended in case no bird-bath scans (azimuthal scans at 90° elevation) are available for Z_{DR} calibration. The method has been applied already at S band (Wang et al. 2017, 2019; Zhang et al. 2020). Trömel et al. (2014a) demonstrated, however, that at C band the dependence of $\alpha_{H/V}$ on the DSD variability is more pronounced and its change with Z_{DR} is nonmonotonic, which further complicates the methodology in addition to the stronger (differential) attenuation and resonance effects at this frequency range compared to S band. Finally, also the coefficients in $R(A_{H/V})$ relations depend more strongly on the DSD at C band. Accordingly, Wang et al. (2017) derived separate $R(A_{H/V})$ relations for three rain types in Taiwan.

Ryzhkov and Zrnić (2019) compared DSDs from the west Pacific area, which is dominated by tropical rain (Thompson et al. 2018), with an Oklahoma disdrometer dataset and found that $R(K_{DP})$ relations may outperform $R(A_{H/V})$ for heavier continental rain, which contains large raindrops originating from large graupel or hail. Thus, combinations of $R(K_{DP})$ and $R(A_{H/V})$ relations at C band are suggested to compensate for shortcomings of the $R(A_{H/V})$ algorithms in rain mixed with hail or rain dominated by very large resonance-size drops. Finally, based on simulations, $R(A_V)$ is less sensitive to DSD variability compared to $R(A_H)$ and may provide higher accuracy in areas of strong attenuation, where Z_h can be buried in noise while Z_v could be still reliably measurable (Diederich et al. 2015b).

In this study, several QPE relations for polarimetric radar observations at C band are derived for Germany using disdrometer observations from the German Meteorological Service (DWD, Deutscher Wetterdienst) and University of Bonn. An optimal combination of $R(A_{H/V})$ and $R(K_{DP})$ relations is explored using radar and rain gauge observations of DWD. The database and applied quality control processes are introduced in section 2 while a modified methodology implying the use of Nw for real-time adjusted $\alpha_{H/V}$ and hybrid QPE algorithms at C band are described in section 3. Section 4 provides an evaluation of the performance of different retrievals, and section 5 discusses potential problems and suggests methods to solve them in the future. Section 6 closes with a summary.

2. Data and quality control

In this study, DSDs measured by local disdrometers are first filtered and smoothed. The processed DSDs are then used to optimize parameters in the ZPHI method and coefficients in rain rate relationships for the regional precipitation climatology. The processing of phase-based radar variables is of utmost importance since the accuracies of both K_{DP} and $A_{H/V}$ are determined by the Φ_{DP} quality. Various QPE products derived from the German C-band weather radar network are evaluated by rain gauge and disdrometer observations, and compared with DWD's operational QPE products, Radar-Online-Aneichung (RADOLAN) RY and RW.

a. Disdrometer data

Northwestern Germany and the coast in the north is under maritime influence while farther inland and toward the south, the climate is more continental. Therefore, measurements of 68 Thies disdrometers of DWD operated within the 150-km range of six DWD C-band radars, namely, Hannover (HNR), Essen (ESS), and Boostedt (BOO) radars in the northwest and Isen (ISN), Memmingen (MEM), and Eisberg (EIS) radars in southeast part of Germany (Fig. 1, purple triangles and dots), are chosen to represent the DSD variability in a transition zone from the European marine regime to the continental regime in Germany. From these disdrometers we selected 30 representative rain days with various types of precipitation between 2015 and 2017 to investigate the impact of the DSD variability on key parameters of QPE retrievals at C band. Together with Thies disdrometer measurements from the rooftop of the Institute for Geosciences, Department of Meteorology at the University of Bonn (Fig. 1, cyan dot) from November 2011 until December 2019, we collected in total 1 020 000 one-minute DSDs.

Thies disdrometers separate the observed particles into 22 diameter (D) and 20 fall velocity (Vt) classes, (Bloemink and Lanzinge 2005) resulting in a D–Vt matrix with 440 bins. Four criteria are employed to filter undesired and unreliable data:

1) Particles with observed Vt deviating from the expected Vt following (Brandes et al. 2002)

$$\mathrm{Vt}(D) = -0.1021 + 4.932D - 0.9551D^2 + 0.079\,34D^3 - 0.002\,362D^4 \quad (1)$$

(D in mm, Vt in m s^{-1}) by a factor 0.5 or more (Tokay et al. 2013) are excluded from the dataset, because they may not be raindrops.
2) Isolated single raindrops without any particles measured in the neighboring eight bins are also removed as outliers. Both criteria resulted in a 30% elimination of particles. The remaining 1-min DSDs are averaged with a 5-min moving-window for noise reduction.
3) Only consecutive 5-min data all reporting as rain are included in the dataset, resulting in 187 211 DSDs.
4) DSDs containing particles identified as solid by the software or rain intensities less than 0.1 mm h^{-1} are also excluded, resulting in 84 169 DSDs.

The DSDs were used in T-matrix simulations (Waterman 1971) to compute the polarimetric variables for a radar wavelength of 5.3 cm (C band), assuming axis ratios following Brandes et al. (2002) and a canting angle distribution with a mean value of 0° and a standard deviation of 8°. All simulations were made for 15°C temperature, because the dependencies of both the intercept parameter of the $R(A_{H/V})$ relations and $\alpha_{H/V}$ on temperature can be ignored (see section 1). Although the largest rain drop diameter reported in Gatlin et al. (2015) is 9.7 mm, our simulations are restricted to diameters below 8 mm, which appears more appropriate for German climate conditions. Apart from various rainfall relations applied in this study [see Eqs. (14)–(19) in section 3b], those simulated polarimetric radar variables are then utilized to derive the $K_{DP}(Z_h)$ relation for the K_{DP} quality assurance, and

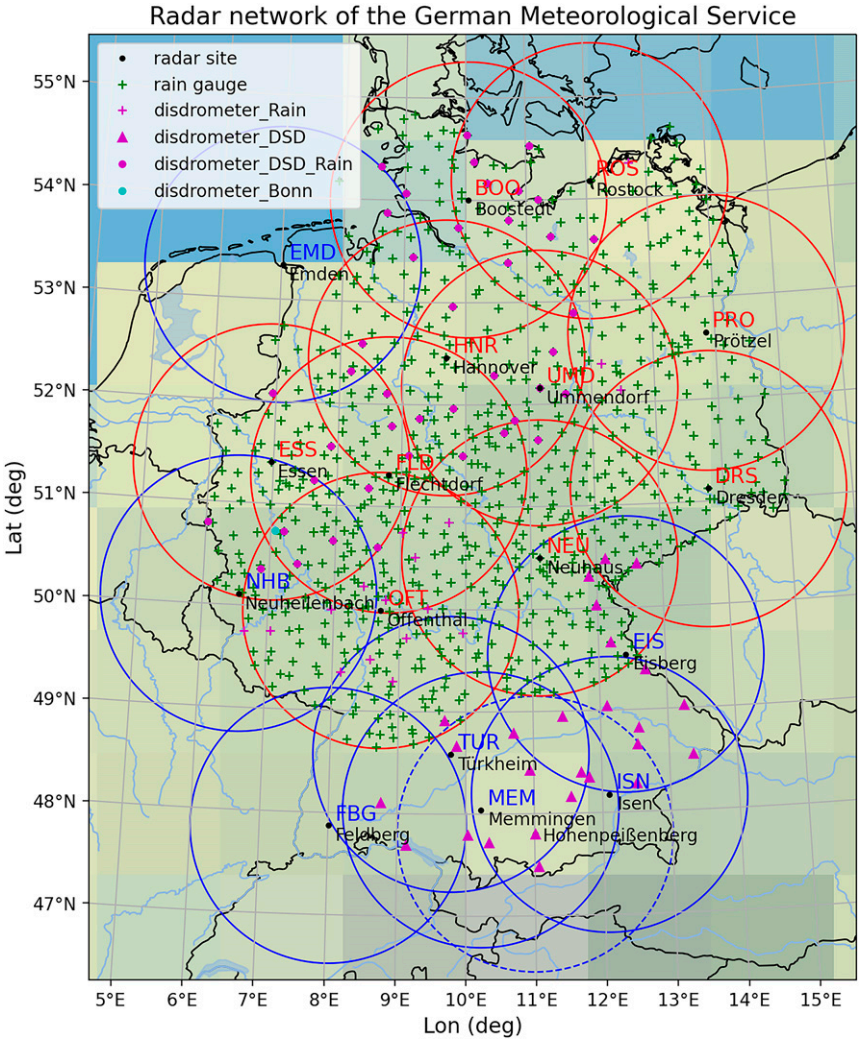

FIG. 1. Spatial coverage of the current radar network of the German Meteorological Service [Deutscher Wetterdienst (DWD)]. Red circles highlight the measurement ranges (150 km) of the radars used in this study, while those for the remaining radars are indicated in blue. The measurement range of the research radar in Hohenpeißenberg is represented with the blue dotted circle. The green/purple crosses mark the rain gauges/Thies disdrometers of DWD used for QPE evaluations. The purple triangles are the DWD disdrometers used for QPE algorithm developments. The purple/cyan dots are the disdrometers of DWD/Institute for Geosciences, Department of Meteorology, University of Bonn for QPE evaluations and algorithm developments.

the $A_{H/V}(Z_{h/v})$ relations for the ZPHI algorithm (see sections 2b and 3a). We also use them to derive DSD-dependent attenuation parameters $\alpha_{H/V}$, defined as the ratio of $A_{H/V}$ and K_{DP}, to better understand and consider their impact on the $R(A_{H/V})$ retrievals (see section 3a).

Additional measurements by 60 Thies disdrometers from DWD (Fig. 1, purple dots and crosses) and the University of Bonn on the case study days (section 2b) serve as rain gauges for QPE evaluations (Fehlmann et al. 2020).

b. *Polarimetric C-band radar data*

Based on a 3-yr dataset, Pejcic et al. (2020, see their Fig. 8) showed that stratiform rain occurs 10 times more frequently than convective rain in Germany. However, even though only 10%–15% of floods occur in summer (Beurton and Thieken 2009), this season shows strong convective precipitation associated with cold fronts and resulting floods are responsible for half of all flood damages in terms of costs/losses in Germany (Zebisch et al. 2005). The demand for accurate radar-based QPE is also emphasized by the expected increase in the probability of heavy rain-induced floods due to climate change (Nissen and Ulbrich 2017) and the relevance of improved flood prediction to mitigate risks to society and ecosystems. In this study, five rain events are examined and the retrievals are analyzed based on observations by 10 DWD C-band radars located in central and northern Germany outlined with red

circles in Fig. 1. These data include four convective events monitored on 19 July 2017, 28 July 2018, 9 August 2018, and 20 July 2019 from 1200 to 2400 UTC, all of which were characterized by organized squall lines and intense rain mixed with small to moderate hail propagating from west to east, and led to severe local flooding. One stratiform event was observed on 25 July 2017 over 24 h and was characterized by widespread intense and continuous rain with embedded convection, which led to severe flooding in the Harz mountain (51°45′N, 10°38′E) range.

The QPE products developed in this work are based on the precipitation scans of the DWD radars, which have a 250-m radial resolution, a 5-min temporal resolution, a 1° beamwidth and a terrain-following elevation angle, which changes azimuthally between 0.6° and 1.5° to avoid deteriorations caused by PBB. The quasi-vertical profile methodology (QVP; Ryzhkov et al. 2016) was used to identify the melting layer (ML) and only observations below the ML were analyzed. Nonmeteorological signals are filtered by removing observations with a copolar correlation coefficient ρ_{HV} below 0.8. Careful processing of Φ_{DP} is required to obtain reliable estimates of $A_{H/V}$ and K_{DP}; especially contributions by the backscatter differential phase δ (Trömel et al. 2013, 2014b), which can be quite strong at C band, need to be mitigated. After an unfolding procedure, our Φ_{DP} processing follows three consecutive steps.

1) Bins with standard deviations of Φ_{DP} above 20° within a moving window of 5 range bins are removed.
2) When the difference between Φ_{DP} and its mean value within a moving window of 17 range bins is larger than 1.25 times the standard deviation of the same window, Φ_{DP} values are replaced by the Φ_{DP} mean (Hubbert and Bringi 1995). This filtering is iterated for up to five times.
3) The resulting Φ_{DP} is smoothed by an unweighted average with a moving window of 5 range bins (Fig. 2b raw/smoothed Φ_{DP} in black/red lines for comparison).

The K_{DP} is retrieved from the filtered Φ_{DP} following Vulpiani et al. (2012). Since nonuniform beam filling and resonance effects from strong cells can cause considerable Φ_{DP} bumps at C band with decreasing ρ_{HV} as shown in Figs. 2a–c in the black rectangles (Ryzhkov and Zrnić 2005), and lead to abnormally high K_{DP} values followed by negative values (Fig. 2d, black line), we substitute K_{DP} by K^*_{DP} (Fig. 2d, red line) defined as

$$K^*_{DP}(r) = \frac{\Delta\Phi_{DP}(r_1, r_2)}{2\int_{r_1}^{r_2}[Z_h(s)]^{0.84}\,ds}[Z_h(r)]^{0.84} \tag{2}$$

in these cases. In Eq. (2) the attenuation-corrected Z_h (mm^6 m^{-3}) and the total span of Φ_{DP} within a range interval (r_1, r_2) $\Delta\Phi_{DP}$ are used (Lim et al. 2013; Zhang et al. 2013). Parameter s is the slant range (km) and the range interval (r_1, r_2) may extend over the entire radar range, or contain only the range interval below the ML, or include only a small rainy radial segment. The exponent 0.84 in Eq. (2) is the exponent in the relation $K_{DP} = 1.6 \times 10^{-4} Z_h^{0.84}$ derived from measured DSDs in Germany (see section 2a) at C band. We replace K_{DP} by K^*_{DP} if 40 dBZ < Z_H < 55 dBZ and $K_{DP} < 0.25°$ km^{-1}. The lower Z_H threshold equals the one used for the application of $R(K_{DP})$ in our hybrid QPE algorithms, while the upper threshold corresponds to the maximum DSD-simulated Z_H in pure rain. The chosen K_{DP} threshold equals the minimum DSD-simulated K_{DP} for $Z_H > 40$ dBZ. In the following, $R(K^*_{DP})$ included in hybrid QPE algorithms denotes the combined use of K_{DP} and K^*_{DP} depending on the conditions fulfilled.

c. *Rain gauge observations and the gauge-adjusted RADOLAN-RW product*

The QPE products derived in this study are evaluated using the measurements of—depending on the event—from 362 to 639 DWD rain gauges (Fig. 1, green crosses). The rain gauges are weighing OTT Pluvio devices, the data of which are available from the DWD Climate Data Center (CDC, https://opendata.dwd.de/climate_environment/CDC/observations_germany/climate/hourly/precipitation/). In addition, we compare our QPE products with DWD's operational 1-km-resolution RADOLAN-RY and RADOLAN-RW products (http://www.dwd.de/RADOLAN), which are based on radar reflectivities only, except of the latter having been adjusted to hourly rain gauge measurements using a weighted average of radar–gauge differences and ratios. In the processing of the RW product, each hour 20% of the gauges are randomly chosen and reserved as audit data, which do not fully contribute to the adjustment.

3. Algorithm development for QPE at C band

Estimates of $A_{H/V}$ from C-band observations for the use in the $R(A_{H/V})$ relations will be based on adaptive $\alpha_{H/V}$ estimators derived from the DSDs via the normalized raindrop concentration (Nw; Testud et al. 2001; Bringi et al. 2003) and the Z_{DR} slope method (section 3a). In addition, the attenuation-based algorithms as well as hybrid QPE estimators including $R(K^*_{DP})$ in heavy rain are proposed (section 3b).

a. *Adaptive attenuation parameters $\alpha_{H/V}$ for the estimation of $A_{H/V}$*

The specific attenuation of horizontally/vertically polarized radar waves ($A_{H/V}$, in dB km^{-1}) cannot be directly measured, but derived from observed $Z_{h/v}$ and Φ_{DP}. Following the ZPHI method proposed by Testud et al. (2000), the radial profile of $A_{H/V}(r)$ within the range interval (r_1, r_2) can be estimated via

$$A_{H/V}(r) = \frac{Z_{ah/v}(r)^{b_{h/v}} C(b_{h/v}, \mathrm{PIA})}{I_{ah/v}(r_1, r_2) + C(b_{h/v}, \mathrm{PIA}) I_{ah/v}(r, r_2)} \tag{3}$$

where

$$I_{ah/v}(r_1, r_2) = 0.46 b_{h/v} \int_{r_1}^{r_2} [Z_{ah/v}(s)]^{b_{h/v}}\,ds, \tag{4}$$

$$I_{ah/v}(r, r_2) = 0.46 b_{h/v} \int_{r}^{r_2} [Z_{ah/v}(s)]^{b_{h/v}}\,ds, \quad \text{and} \tag{5}$$

$$C(b_{h/v}, \mathrm{PIA}) = \exp(0.23 b_{h/v} \mathrm{PIA}) - 1. \tag{6}$$

In Eqs. (3)–(6), $Z_{ah/v}$ is the measured, uncorrected apparent reflectivity at horizontal h or vertical v polarization (mm^6 m^{-3}), $b_{h/v}$ is the exponent in the relation $A_H = 1.2 \times 10^{-5} Z_h^{0.86}$ or

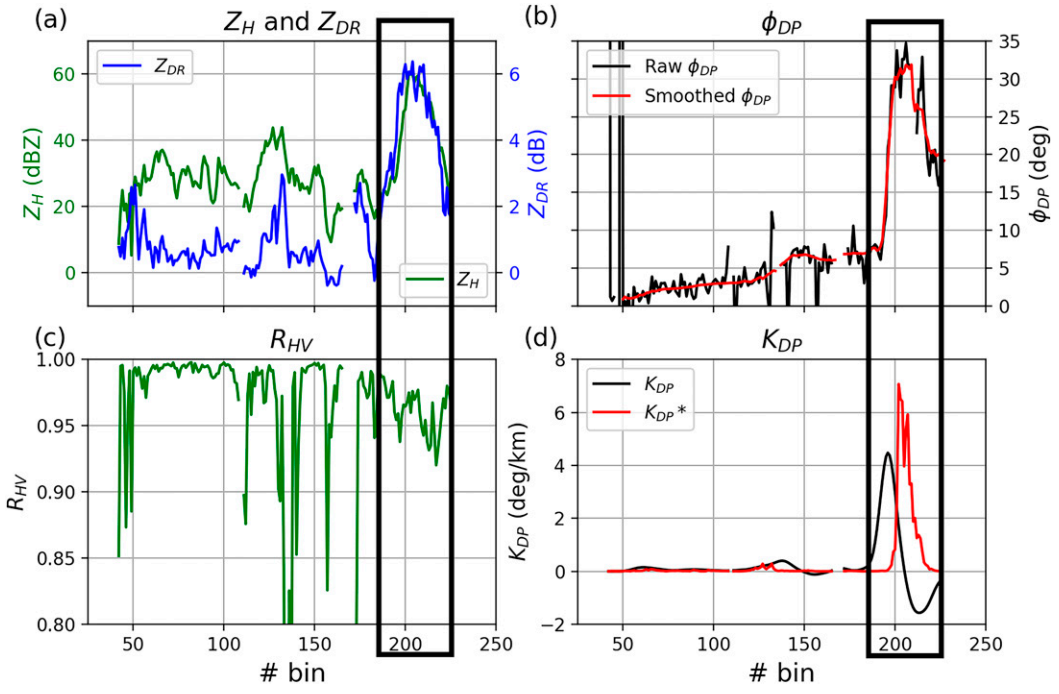

FIG. 2. The radial profiles of radar variables from the ray at 66.5° azimuth of the OFT radar at 1510 UTC 28 Jul 2018, including (a) Z_H in green and Z_{DR} in blue after first-guess attenuation correction, (b) raw Φ_{DP} in black and smoothed Φ_{DP} in red, (c) ρ_{HV}, and (d) K_{DP} in black and the substitute K_{DP}, i.e., K_{DP}^*, in red.

$A_V = 1.3 \times 10^{-5} Z_v^{0.87}$ derived from measured DSDs (see section 2a) and assumed to be a constant at C band, and PIA is the path-integrated attenuation within (r_1, r_2) estimated from $\Delta\Phi_{DP}$ as

$$\text{PIA} = \alpha_{H/V}[\Phi_{DP}(r_2) - \Phi_{DP}(r_1)] = \alpha_{H/V}\Delta\Phi_{DP}, \quad (7)$$

with the attenuation parameter $\alpha_{H/V}$. The average value of α_H at C band is around 0.08 dB per degree but $\alpha_{H/V}$ can vary with the DSDs from about 0.05 to 0.18 dB per degree (Trömel et al. 2014a). Wang et al. (2019) and Zhang et al. (2020) estimated DSD-dependent α_H values at S band from the Z_{DR} slope (see section 1). For our C-band algorithm development based on the disdrometer-observed DSDs, we first stratify the observations according to Nw, which serves as a proxy for different precipitation classes, then the $\alpha_{H/V}$ estimators are derived from the Z_{DR} slopes and representative $\alpha_{H/V}$ values of each class. Nw ($\text{m}^{-3}\,\text{mm}^{-1}$) is defined as

$$\text{Nw} = \frac{4^4}{\pi\rho_w}\frac{10^3\text{LWC}}{D_m^4}, \quad (8)$$

where

$$\text{LWC} = \frac{\pi}{6} \times \rho_w \int_{0.125}^{8} N(D) D^3\, dD, \quad (9)$$

$$D_m = \frac{\int_{0.125}^{8} N(D) D^4\, dD}{\int_{0.125}^{8} N(D) D^3\, dD}, \quad (10)$$

and ρ_w is the density of water ($1.0\,\text{g}\,\text{cm}^{-3}$). Both LWC (liquid water content in $\text{g}\,\text{m}^{-3}$) and D_m (mass-weighted mean diameter in mm) are calculated from measured DSDs. The term $N(D)$ is the number of raindrops per unit volume per unit size interval ($\text{m}^{-3}\,\text{mm}^{-1}$).

We separate the dataset into eight Nw classes using the 10th, 20th, 30th, 40th, 50th, 65th, and 80th percentiles as thresholds (Fig. 3). Small Nw values indicate a relatively high fraction of larger drops, which may occur in the preconvective regime of continental rain or midlatitude frontal rain, while high values are typical for tropical rain formed predominantly via warm rain process or deep continental showers with abundant smaller raindrops (Tokay et al. 2008). For each Nw class, representative $\alpha_{H/V}$ values are estimated via the relation $A_{H/V} = \alpha_{H/V} K_{DP}$, which best fits the data with $A_{H/V}$ and K_{DP} simulated from the DSDs. We exclude data with $Z_H > 40$ dBZ because α_H is highly variable in this range due to the resonance effects at C band (Carey and Petersen 2015) (and our hybrid QPEs approach this range via K_{DP}-based estimators). The Z_{DR} slope (K_H, in dB dBZ^{-1}) of each class is calculated as

$$K_H = \frac{Z_{DR\_40} - Z_{DR\_25}}{\Delta Z_H}, \quad (11)$$

where Z_{DR_25} and Z_{DR_40} are the medians of the simulated Z_{DR} for $Z_H = 25 \pm 1$ dBZ and 40 ± 1 dBZ, respectively. Here, we modify the considered Z_H range from (20 dBZ, 50 dBZ) (Wang et al. 2017, 2019) to (25 dBZ, 40 dBZ) because of the less pronounced resonance effects and the reduced occurrence

of $Z_H > 40$ dBZ in stratiform rain in Germany. Besides, for the overwhelming majority of points within this range, the dependence of Z_{DR} on Z_H is almost quasi-linear although with a varying slope depending on Nw (Fig. 4a). The K_H values for the lower Nw classes are higher, and vice versa. In the last step, the relationships between the derived $\alpha_{H/V}$ and K_H values are estimated as ratios of polynomial functions:

$$\alpha_H = \frac{1.36 - 7.17 \times 10^1 K_H + 1.36 \times 10^3 K_H^2}{1 \times 10^1 - 7.03 \times 10^2 K_H + 1.57 \times 10^4 K_H^2}, \quad \text{and} \quad (12)$$

$$\alpha_V = \frac{1.05 - 5.35 \times 10^1 K_H + 8.40 \times 10^2 K_H^2}{1 \times 10^1 - 6.21 \times 10^2 K_H + 1.12 \times 10^4 K_H^2}. \quad (13)$$

We do not consider the last class (Nw > 80th percentile) when deriving Eqs. (12) and (13) since Z_H in this class are mostly below 30 dBZ, away from 40 dBZ to derive the corresponding K_H value. Both α_H and α_V first decrease with K_H and then remain constant (Fig. 4b). If the data with $Z_H >$ 40 dBZ are included in the fit, α_H first decreases but grows again with increasing K_H (Fig. 4b, dashed line).

When applying the algorithms to real radar observations, we first estimate K_H for each azimuthal radar scan via the following procedure.

1) A first-guess (differential) attenuation correction is applied to Z_H and Z_{DR} using default values derived from the entire DSD dataset (0.093 dB per degree for α_H, and 0.021 dB per degree for β which is the ratio of specific differential attenuation A_{DP} and K_{DP}).
2) Radar bins with $\Phi_{DP} > 30°$ are excluded from the $\alpha_{H/V}$ estimation in order to reduce attenuation-related uncertainties.
3) For each azimuth scan, K_H is estimated by fitting a straight line to the median Z_{DR} values derived with more than 100 samples for each 1-dBZ interval of Z_H between 25 and 40 dBZ. The K_H is limited to values above 0.035 dB dBZ^{-1} to avoid unrealistically high $\alpha_{H/V}$ values.
4) Then the values of $\alpha_{H/V}$ are derived via Eqs. (12) and (13) for each scan. If the maximum valid interval of Z_H for fitting is below 30 dBZ, values of $\alpha_H = 0.153$ dB per degree and $\alpha_V = 0.147$ dB per degree derived from the last Nw class are applied.
5) The $\alpha_{H/V}$ estimates are renewed for each scan if more than 30 000 valid data points are available.

We also try to mitigate hail contamination in heavy rain and effects of noisy Φ_{DP} in stratiform rain. Following Wang et al. (2017, 2019), ranges with $Z_H > 50$ dBZ (potential existence of hail) are excluded from the integration path in the ZPHI method to avoid extremely high $A_{H/V}$ values and gross overestimations of rainfall rates. If a total span of Φ_{DP}, i.e., $\Delta\Phi_{DP}$, in Eq. (7) remains below 10°, we replace it by the mean of the four closest rays.

b. The set of rainfall retrievals for C-band radars

We derived the following rainfall rate relations from our DSD dataset:

$$R(Z_h) = 0.052 Z_h^{0.57}, \quad (14)$$

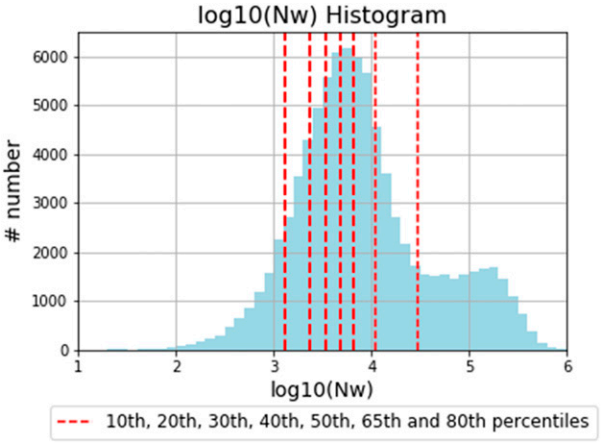

FIG. 3. Histogram of the normalized raindrop concentration (Nw; m^{-3} mm^{-1}; logarithmic scale) derived from 84 169 drop size distributions (DSDs) measured by Thies disdrometers from DWD (2015–17) and the Institute for Geosciences, Department of Meteorology, University of Bonn (2012–19). The red dashed lines indicate the 10th, 20th, 30th, 40th, 50th, 65th, and 80th percentiles of Nw.

$$R(K_{DP}) = 20.7 K_{DP}^{0.72}, \quad (15)$$

$$R(A_H)^a = 121 A_H^{0.74}, \quad (16)$$

$$R(A_V)^a = 193 A_V^{0.82}, \quad (17)$$

$$R(A_H)^b = 307 A_H^{0.92}, \quad \text{and} \quad (18)$$

$$R(A_V)^b = 452 A_V^{0.98}. \quad (19)$$

These relations are obtained via the Levenberg–Marquardt (LM) algorithm (Levenberg 1944), which is less impacted by the much more frequent, lower-intensity observations and offers a better fit in more relevant heavy rain. While the $R(Z_h)$ and $R(A_{H/V})^a$ relations have been derived based on the entire dataset, only data with $Z_H >$ 40 dBZ were used for the derivation of the $R(K_{DP})$ relation and data with $Z_H < 40$ dBZ for $R(A_{H/V})^b$.

Based on the six rainfall relations above, we introduce a set of nine precipitation retrieval algorithms for the German C-band radars (Table 1):

1) a rainfall retrieval based on Z_h;
2) a hybrid retrieval based on Z_h and combined with a $R(K_{DP})$ retrieval when $Z_H > 40$ dBZ;
3) a similar retrieval as algorithm 2 but instead of $R(K_{DP})$ the optimized $R(K_{DP}^*)$ is used;
4) a retrieval based on A_H with a fixed α_H value;
5) a hybrid retrieval based on A_H with a fixed α_H value but replaced by $R(K_{DP}^*)$ for $Z_H > 40$ dBZ;
6) a hybrid retrieval based on $A_H^{adj.}$ with scan-wise adjusted α_H values but replaced by $R(K_{DP}^*)$ when $Z_H > 40$ dBZ;
7) same as algorithm 4, but based on A_V;
8) same as algorithm 5, but based on A_V; and
9) same as algorithm 6, but based on A_V.

All $R(Z_h)$ rainfall retrievals are based on Z_h (mm^6 m^{-3}) with a first-guess attenuation correction ($\alpha_H = 0.093$ dB per degree

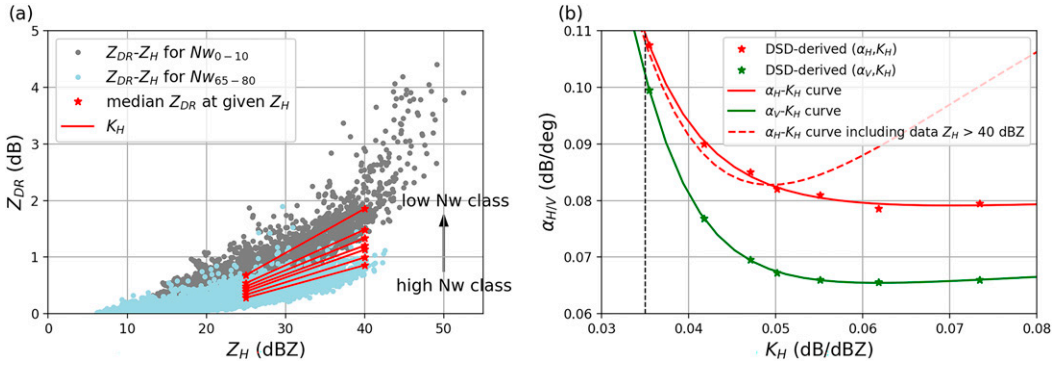

FIG. 4. (a) The slopes of Z_{DR} vs Z_H, named K_H, for seven DSD classes defined via the percentiles of Nw (see Fig. 3). Gray and light blue dots are DSD-simulated data from the classes in the 0th–10th and 65th–80th percentile intervals of Nw. Red lines are K_H and red stars mark the median Z_{DR} for Z_H at 25 and 40 dBZ within ±1-dBZ width. (b) Curves of K_H vs $\alpha_{H/V}$ for the horizontal (red) and vertical (green) polarization, respectively. The red dashed line is the curve of K_H vs α_H derived from the dataset including $Z > 40$ dBZ. The red/greens stars mark the $\alpha_{H/V}$ values derived based on DSDs from the seven rain-type classes.

and $\alpha_V = 0.071$ dB per degree derived from the entire DSD dataset) and hybrid retrievals are combined with a $R(K_{DP})$ or $R(K^*_{DP})$ [see Eq. (2)] retrieval when the attenuation-corrected Z_H exceeds 40 dBZ. For pure $A_{H/V}$-based retrieval algorithms 4 and 7, Eqs. (16) and (17) are used, or else Eqs. (18) and (19) are applied for hybrid $A_{H/V}$-based retrievals. Retrieval $R(Z_h)/R(K_{DP})$ is used as a benchmark algorithm (because of its frequent use) to qualify the developments presented in this study. All QPE products are provided for radar observations below the ML.

4. Results

For the evaluation of the quality of the retrievals, we compare hourly and event-accumulated rainfall sums computed from radar-derived QPE retrievals and the RADOLAN RY and RW products of DWD against rain gauge and disdrometer measurements via the normalized mean bias (NMB), normalized root-mean-square error (RMSE), and Pearson's correlation coefficient (CC) defined as

$$\mathrm{NMB} = \frac{\sum_{i=1}^{N}(R_i - G_i)}{\frac{N}{\overline{G}}} \times 100\%, \tag{20}$$

$$\mathrm{NRMSE} = \frac{\sqrt{\frac{\sum_{i=1}^{N}(R_i - G_i)^2}{N}}}{\sigma(G)} \times 100\%, \quad \text{and} \tag{21}$$

$$\mathrm{CC} = \frac{\sum_{i=1}^{N}(R_i - \overline{R})(G_i - \overline{G})}{\sqrt{\sum_{i=1}^{N}(R_i - \overline{R})^2 \sum_{i=1}^{N}(G_i - \overline{G})^2}}. \tag{22}$$

In Eqs. (20)–(22), N is the total number of QPE–gauge (or QPE–disdrometer) pairs compared; R_i and G_i are, respectively, the radar-estimated and rain gauge (or disdrometer) observed rainfall sums at the ith station; $\overline{R}$ and $\overline{G}$ are the mean values of R and G; and $\sigma(G)$ is the standard deviation of G. We

TABLE 1. A set of precipitation retrieval algorithms for the German C-band radars, including three retrievals based on $R(Z_h)$ with a first-guess attenuation correction ($\alpha_H = 0.093$ dB per degree and $\alpha_V = 0.071$ dB per degree derived from the entire DSD dataset), three A_H-based and three A_V-based rainfall retrievals. The hybrid retrievals are combined with $R(K_{DP})$ or $R(K^*_{DP})$, which mitigates—among others—effects of Φ_{DP} bumps [see Eq. (2)], when the attenuation-corrected Z_H exceeds 40 dBZ. Note that $R(K^*_{DP})$ denotes the combined use of K^*_{DP} (if 40 dB$Z < Z_H < 55$ dBZ and $K_{DP} < 0.25°\,\mathrm{km}^{-1}$) and K_{DP} (elsewhere if $Z_H > 40$ dBZ). All QPE products are provided only for radar observations below the ML.

Rainfall retrievals	Description	Equations
$R(Z_h)$	A rainfall retrieval based on Z_h	(14)
$R(Z_h)/R(K_{DP})$	A hybrid retrieval based on Z_h and combined with $R(K_{DP})$	(14), (15)
$R(Z_h)/R(K^*_{DP})$	A hybrid retrieval based on Z_h and combined with $R(K^*_{DP})$	(14), (15)
$R(A_H)$	A retrieval based on A_H with a fixed α_H value	(16)
$R(A_H)/R(K^*_{DP})$	A hybrid retrieval based on A_H with a fixed α_H value and combined with $R(K^*_{DP})$	(18), (15)
$R(A_H^{adj.})/R(K^*_{DP})$	A hybrid retrieval based on $A_H^{adj.}$ with scan-wise adjusted α_H values and combined with $R(K^*_{DP})$	(18), (15)
$R(A_V)$	A retrieval based on A_V with a fixed α_V value	(17)
$R(A_V)/R(K^*_{DP})$	A hybrid retrieval based on A_V with a fixed α_V value and combined with $R(K^*_{DP})$	(19), (15)
$R(A_V^{adj.})/R(K^*_{DP})$	A hybrid retrieval based on $A_V^{adj.}$ with scan-wise adjusted α_V values and combined with $R(K^*_{DP})$	(19), (15)

TABLE 2. Normalized mean bias (NMB), normalized root-mean-square error (NRMSE), and Pearson's correlation coefficient (CC) for nine QPE products evaluated against rain gauge measurements for 1- and 12-/24-hourly accumulations (h_i with i for number of hours) for five rain events. Bold (italic) numbers mark algorithms with the top (second) quality measures from our retrievals (RY is not included in the ratings). Only hourly NMB is provided because it is independent of accumulation span. The total number N_1, N_{12}, and N_{24} of data points available for the evaluation with rain gauges for 1-, 12-, and 24-hourly accumulations, respectively, are also noted.

Score	h_i	$R(Z_h)$	$R(Z_h)/R(K_{DP})$	$R(Z_h)/R(K^*_{DP})$	$R(A_H)$	$R(A_H)/R(K^*_{DP})$	$R(A_H^{adj.})/R(K^*_{DP})$	$R(A_V)$	$R(A_V)/R(K^*_{DP})$	$R(A_V^{adj.})/R(K^*_{DP})$	RY
19 July 2017 (convective event from 1200 to 2400 UTC; N_1 = 1590; N_{12} = 639)											
NMB (%)	h_1	18.7	**8.3**	12.5	18.3	20.5	12.4	22.9	14.7	***11.9***	16.9
NRMSE (%)	h_1	77.7	**68.1**	***68.7***	76.8	72.0	69.9	78.3	69.7	69.1	75.2
	h_{12}	65.7	**56.1**	56.9	62.4	63.1	57.6	64.4	57.6	***56.2***	68.7
CC	h_1	0.71	0.75	0.75	0.72	0.74	0.74	0.74	0.75	0.75	0.69
	h_{12}	0.83	0.85	0.85	0.85	0.84	0.85.	0.87	0.86	0.86	0.78
28 July 2018 (convective event from 1200 to 2400 UTC; N_1 = 1539; N_{12} = 616)											
NMB (%)	h_1	**−0.4**	−8.5	−2.9	11.8	9.4	***1.8***	19.7	5.1	***1.8***	30.2
NRMSE (%)	h_1	80.5	73.4	**71.9**	78.4	73.3	72.4	83.4	72.6	***72.0***	82.9
	h_{12}	62.7	56.5	***53.5***	58.6	56.9	53.6	61.4	54.0	**52.6**	79.3
CC	h_1	0.67	0.71	0.73	0.71	0.73	0.73	0.72	0.73	0.73	0.68
	h_{12}	0.82	0.85	0.87	0.86	0.86	0.87	0.88	0.87	0.87	0.78
9 August 2018 (convective event from 1200 to 2400 UTC; N_1 = 1628; N_{12} = 753)											
NMB (%)	h_1	−13.8	−13.5	−9.2	***1.2***	3.6	−2.6	7.1	**−1.1**	−2.4	16.3
NRMSE (%)	h_1	77.1	***70.5***	**70.4**	73.9	71.3	70.7	76.1	70.8	70.7	76.7
	h_{12}	61.5	***50.8***	**50.2**	53.2	53.6	51.9	54.8	51.8	52.0	69.5
CC	h_1	0.71	0.76	0.76	0.74	0.76	0.76	0.75	0.76	0.76	0.72
	h_{12}	0.79	0.86	0.86	0.85	0.85	0.85	0.86	0.86	0.85	0.76
20 July 2019 (convective event from 1200 to 2400 UTC; N_1 = 1765; N_{12} = 614)											
NMB (%)	h_1	6.6	−4.5	**−0.5**	11.8	11.3	***2.9***	17.7	7.0	3.3	36.3
NRMSE (%)	h_1	88.8	**72.5**	***73.3***	87.8	77.1	75.3	94.6	75.9	75.3	97.7
	h_{12}	65.8	***49.9***	**49.6**	64.6	57.3	52.5	71.8	53.7	52.5	91.2
CC	h_1	0.67	0.74	0.74	0.70	0.74	0.73	0.71	0.74	0.74	0.67
	h_{12}	0.80	0.86	0.87	0.83	0.86	0.86	0.84	0.86	0.86	0.80
25 July 2017 (stratiform event from 0000 to 2400 UTC; N_1 = 5501; N_{24} = 362)											
NMB (%)	h_1	−31.0	***−28.2***	**−27.8**	−34.9	−41.0	−45.3	−47.2	−52.4	−51.3	−10.4
NRMSE (%)	h_1	64.3	***62.5***	**62.0**	63.6	65.3	68.2	70.6	72.8	71.9	59.7
	h_{24}	66.4	***61.6***	**61.1**	68.8	76.0	82.3	85.4	92.2	90.8	47.5
CC	h_1	0.81	0.82	0.82	0.82	0.82	0.82	0.82	0.82	0.82	0.78
	h_{24}	0.86	0.88	0.88	0.89	0.89	0.89	0.89	0.88	0.88	0.86

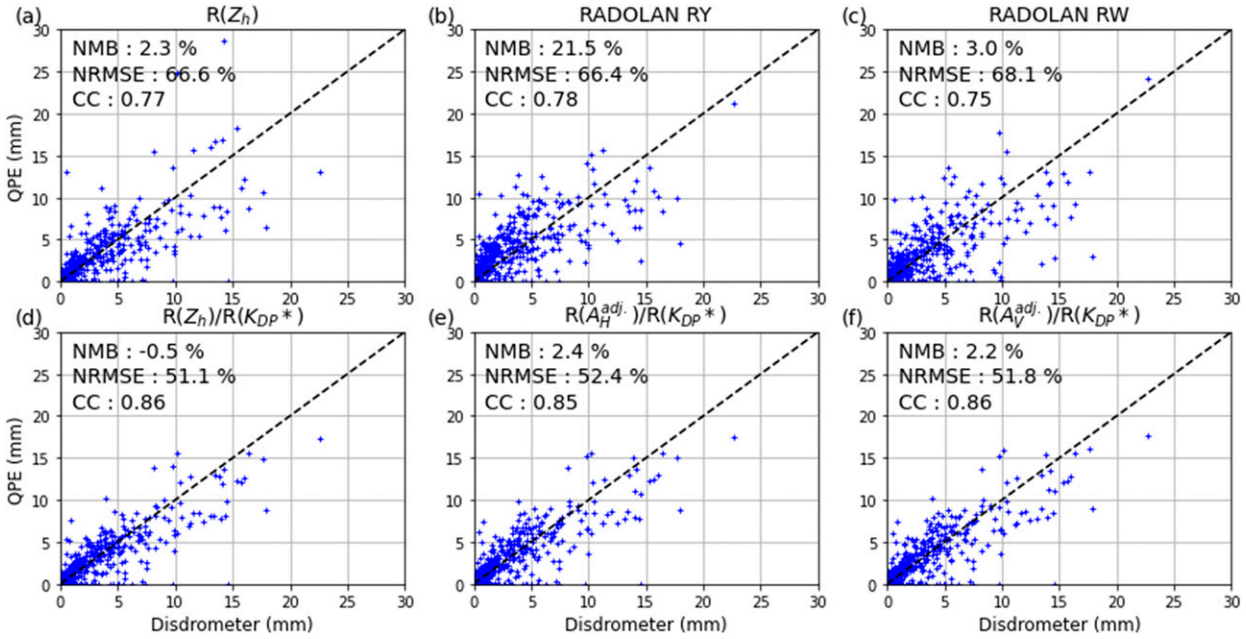

FIG. 5. Scatterplots of hourly accumulated rainfall derived from (a) $R(Z_h)$, (b) RY, (c) RW, (d) $R(Z_h)/R(K^*_{DP})$, (e) $R(A^{adj.}_H)/R(K^*_{DP})$, and (f) $R(A^{adj.}_V)/R(K^*_{DP})$ vs rainfall measured by disdrometers from four convective events. The total number of data points is 504.

first evaluate the observations during the four convective events followed by the one long-lasting stratiform event. The evaluation statistics for all nine algorithms and the RADOLAN RY product from five events are summarized in Table 2, to which we refer in the following subsections.

a. Convective rain

When compared with the rain gauge observations, the $R(Z_h)$ algorithm has as expected relatively higher NRMSE and the lowest CC for all cases. For pure $A_{H/V}$-based algorithms, $R(A_H)$ shows better performance in terms of NMB and NRMSE but CC when compared to $R(A_V)$. Significant overestimation of $R(A_V)$ may result from the larger impact of hail-mixed rain on $R(A_V)$. Values improve when $R(K_{DP})$ or $R(K^*_{DP})$ substitute for high reflectivities. Especially the use of K^*_{DP} reduces the underestimation in heavy rain in Z_h estimates. The $R(A_H)/R(K^*_{DP})$ algorithm always shows larger NMB than $R(A_V)/R(K^*_{DP})$. The use of $A^{adj.}_{H/V}$ reduces the NMB compared to the use of $A_{H/V}$ with the improvement being more pronounced for the horizontal polarization; thus $R(A^{adj.}_H)/R(K^*_{DP})$ reveals a performance comparable to $R(A^{adj.}_V)/R(K^*_{DP})$, which demonstrates that the scan-wise adjustment of $\alpha_{H/V}$ plays a role and successfully reduces the DSD impact on $R(A_H)$. The error numbers of both $R(A^{adj.}_H)/R(K^*_{DP})$ and $R(A^{adj.}_V)/R(K^*_{DP})$ are close to $R(Z_h)/R(K^*_{DP})$. When comparing our QPE products with the operational RY and RW products (Fig. 5), we use the disdrometer observations instead of the gauges, because the latter were potentially used in the RW product. Especially

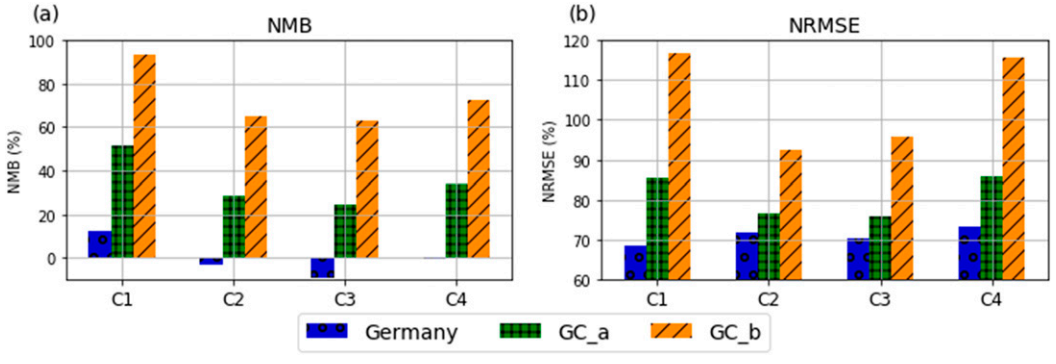

FIG. 6. The comparison of (a) NMB and (b) NRMSE for the $R(Z_h)/R(K^*_{DP})$ retrievals evaluated by rain gauge measurements for hourly accumulations. The blue bars represent the algorithms derived from DSD measurements in Germany, and the green and orange bars are the algorithms proposed by Gou and Chen (2021) [Eqs. (5a)–(5d) in their paper] for two convective events. C1–C4 indicate the convective events ordered by time.

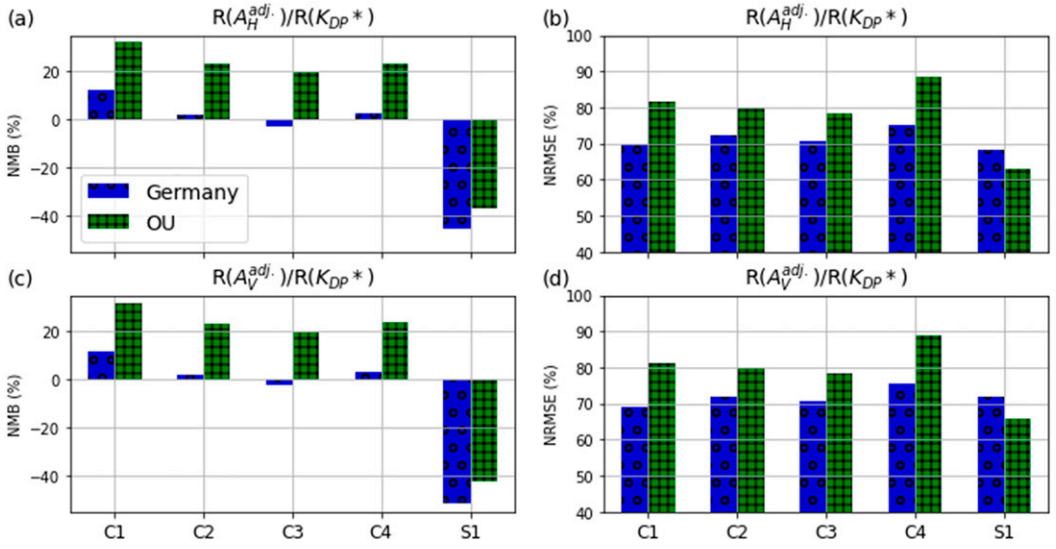

FIG. 7. The comparison of (a),(c) NMB and (b),(d) NRMSE for the $R(A_H^{adj.})/R(K_{DP}^*)$ and $R(A_V^{adj.})/R(K_{DP}^*)$ retrievals evaluated by rain gauge measurements for hourly accumulations. The blue and green bars represent the algorithms derived from DSD measurements in Germany and Oklahoma. C1–C4 indicate the convective events ordered by time, and S1 is the stratiform event.

the hybrid QPEs outperform RY and even RW with lower NRMSE and higher CC values. If we consider the underestimation of Thies-measured rainfall (Fehlmann et al. 2020) and take RW's NMB value as a reference, $R(A_H^{adj.})/R(K_{DP}^*)$ and $R(A_V^{adj.})/R(K_{DP}^*)$ have slightly closer NMB values to RW than $R(Z_h)/R(K_{DP}^*)$. Thus, according to the evaluation of disdrometer measurements, state-of-the-art polarimetric rainfall retrievals give a chance to provide near-real-time QPE products with a higher accuracy than nonpolarimetric QPE products with rain gauge adjustment on an hourly basis.

We also compare our QPE algorithms with the ones in the existing literature. For the $R(Z_h)/R(K_{DP}^*)$ algorithms, two sets of $R(Z_h)$ relation (derived using data with $Z_H < 40$ dBZ) combined with $R(K_{DP})$ relation for two convective rain events proposed by Gou and Chen (2021) [see Eqs. (5a)–(5d) in their paper] are used. The results show a strong overestimation of rainfall and large NRMSE values no matter which relation set is applied (Fig. 6). According to Table 10.3 of Ryzhkov and Zrnić (2019), an intercept of $R(K_{DP})$ relation may vary from 20 to 35 being generally higher for tropical rain. The intercept in Eq. (15) is at the lower end and smaller than Gou and Chen (2021) which can be attributed to a more tropical rain in eastern China. For the $R(A_{H/V}^{adj.})/R(K_{DP}^*)$ algorithms, when compared to the relations based on DSD measurements in Oklahoma, $R = 294A_H^{0.89}$, $R = 393A_V^{0.93}$, and $R = 25.3K_{DP}^{0.78}$ (Ryzhkov et al. 2014; Ryzhkov and Zrnić 2019), our QPE products derived from local DSD measurements show significantly less biases and smaller NRMSE values (Fig. 7).

b. Stratiform rain

For the stratiform situation, rainfall retrievals based on Z_h clearly outperform the retrievals based on $A_{H/V}$ (Table 2) and improvement by using $R(K_{DP}^*)$ for higher rain rates is limited. The underestimation by $A_{H/V}$-based retrievals may originate from the smoothing process of Φ_{DP} and too low $\alpha_{H/V}$ values, and scan-wise $\alpha_{H/V}$ adjustments do not really improve the results. Retrievals of Oklahoma also lead to noticeably underestimated rainfall in this event (Fig. 7).

The impact of PBB in the Z_h-based products is obvious in the observations of the Hannover (HNR) and Rostock (ROS) radars [Fig. 8a RW and Fig. 8b $R(Z_h)/R(K_{DP}^*)$ shown with black arrows], but not for $A_{H/V}$-based QPE as expected (Figs. 8c–d). Note that some radar coverages deviate from the circular shape due to the terrain-following scan strategy and the restriction of our retrievals to observations below the ML. Especially in the mountainous southern part of Germany, where PBB cannot be completely avoided by the terrain-following scan strategy, great benefits can be expected from the application of $R(A_{H/V})$.

5. Discussion

The improvement of $A_{H/V}^{adj.}$ is achieved only by reducing the bias and there is still an overestimation in one of convective cases and, in particular, an underestimation in the stratiform case. This can be explained by the fact that a scan-wise $\alpha_{H/V}$ represents an average value but cannot distinguish between different precipitation types occurring within a scan. In the ZPHI method, an improper $\alpha_{H/V}$ value leads to an erroneous estimation of PIA from Φ_{DP} and thus to an incorrect $A_{H/V}$ [or $R(A_{H/V})$] along a ray. If the interquartile ranges and mean values of Z_H (below 40 dBZ) are used to demonstrate how evenly different rain intensities distribute within the scans where a scan-wise $\alpha_{H/V}$ is applied (Fig. 9), we could find that QPE retrievals of cases with low interquartile ranges and relatively high/low mean values of Z_H, that is the convective event on 19 July 2017 and the stratiform event, show larger NMB values. For example, in the stratiform case with the NMB values around 50%, we found that more than 90% of data (from the UMD radar for example) are below 30 dBZ, and the

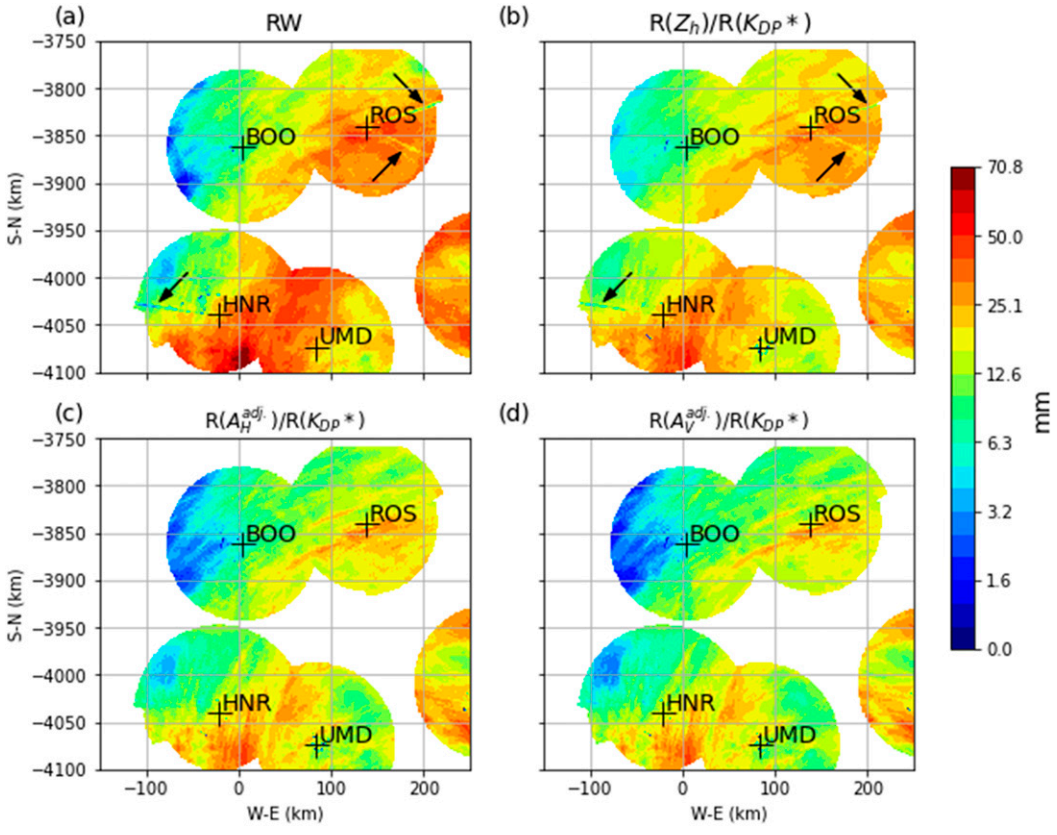

FIG. 8. Daily accumulated rainfall composite maps of the stratiform rain event on 25 Jul 2017 from (a) RW, (b) $R(Z_h)/R(K_{DP}^*)$, (c) $R(A_H^{adj.})/R(K_{DP}^*)$, and (d) $R(A_V^{adj.})/R(K_{DP}^*)$. The black arrows indicate the rays affected by partial beam blockage (PBB).

rest of higher Z_H with higher Z_{DR} (a mean value of 0.79 dB corresponding to the fourth Nw class) from embedded convection strongly dominate the fitting of Z_{DR} slope, K_H. Lower $\alpha_{H/V}$ values were thus estimated from higher K_H values and led to an underestimation of rainfall. According to the studies in the United States (e.g., Wang et al. 2019), a similar tendency of the S-band $R(A_H)$ algorithm with a single scan-wise value of α to overestimate heavier convective rain and underestimate lighter stratiform rain was observed in the situations when convective and stratiform rain coexist in the radar field of view. If we apply the fixed α_H and α_V values, respectively, from the last Nw class to A_H and A_V estimates during the whole event, the results shown in Fig. 10 with blue dots are much more convincing. As a result, an optimization of net $\alpha_{H/V}$ along individual rays or within segments of rays is suggested for future work. Even more promising is the use of a rain-type classifier

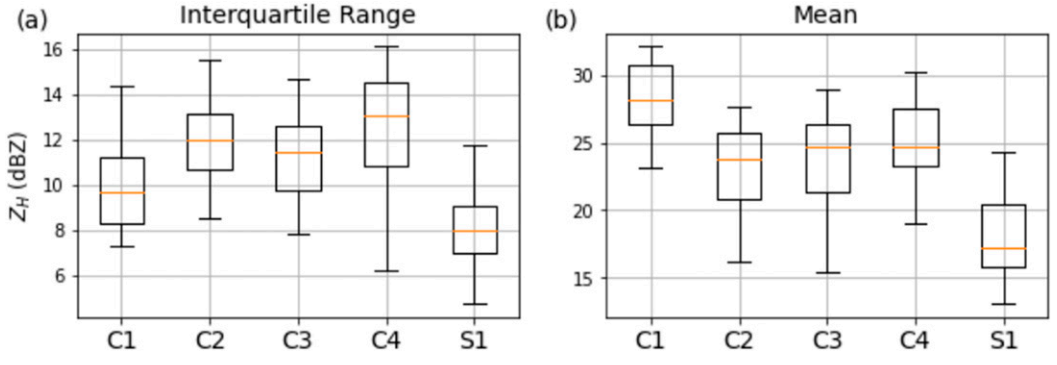

FIG. 9. The boxplots of (a) interquartile ranges and (b) mean values of Z_H from each scan for four convective (C1–C4) and one stratiform (S1) rain events.

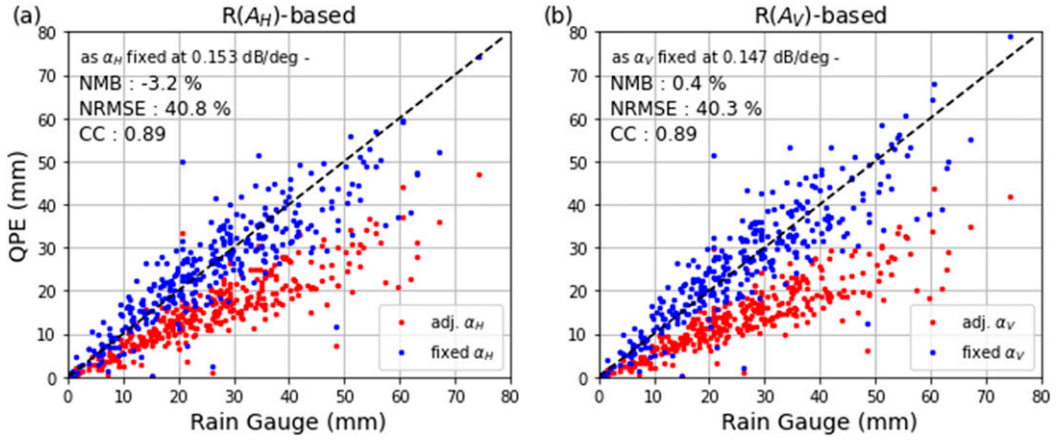

FIG. 10. The scatterplots of stratiform event accumulated rainfall derived from (a) $R(A_H^{\text{adj.}})/R(K_{\text{DP}}^*)$ and $R(A_H)/R(K_{\text{DP}}^*)$ with a fixed α_H value as 0.153 dB per degree vs rain gauge measurements, and (b) $R(A_V^{\text{adj.}})/R(K_{\text{DP}}^*)$ and $R(A_V)/R(K_{\text{DP}}^*)$ with a fixed α_V value as 0.147 dB per degree. The total number of data points is 939.

on the whole scan and adjusting $\alpha_{H/V}$ separately for the different classes.

As an example result of the different algorithms, we present in Figs. 11a and 11b instantaneous rainfall maps derived from observations of the HNR radar and produced by the best estimators using Z_h, and $A_V^{\text{adj.}}$ combined with a K_{DP}-based estimator. In areas right behind the strongly attenuating hail cores, all products show several bundles of rays with clearly underestimated rain rates, in particular for the $R(A_V^{\text{adj.}})$-based algorithm, which should be immune to attenuation effects. It is found that the exclusion of hail or intense convective cells (Figs. 11c,d, range within black dashed lines, defined as $Z_H > 50$ dBZ) from the integration path unbalances the distribution of PIA. Namely, if we simply connect two pure-rain segments as one, the attenuation from the intense cell will be missed by reduced Φ_{DP} and little PIA will be distributed incorrectly to the bins behind. It could lead to an overestimation of $A_{H/V}$ before and an underestimation after the hot spot, which is clearly indicated by the comparison of $A_V^{\text{adj.}}$ and low-resolved K_{DP}-derived A_V ($A_V^{\text{KDP}} = \alpha_V K_{\text{DP}}$ with a scan-wise α_V = 0.066 dB per degree) (Fig. 11d, blue and green lines) if we focus on the regions $Z < 40$ dBZ. Especially for the shorter wavelength radars with pronounced attenuation effect, the segments behind the hot spot are badly affected. Therefore, the integral process should be reset in each pure-rain segment for the ZPHI method.

6. Summary and conclusions

We derived new polarimetric rainfall algorithms for C band radars from T-matrix simulations applied to a large DSD dataset collected over Germany. The classification of DSDs and radar observations group according to Nw and Z_{DR} slope have been exploited to optimize $\alpha_{H/V}$ (required for the estimation of $A_{H/V}$ via the ZPHI method). Several rainfall retrievals for DWDs C-band radars were evaluated with rain gauge and disdrometer measurements, and compared with the operational Z_h-based RADOLAN RY and RW products. We concentrated our analysis on four hail-bearing storms and a widespread stratiform case. This paper presents the first application of regime-adapted rainfall retrievals using $A_{H/V}$ to a C-band radar network in Europe.

For the convective cases, the algorithms using $R(K_{\text{DP}}^*)$ for higher rain rates have less biases in moderate and heavy rain compared to $R(K_{\text{DP}})$. Overall, rainfall retrievals using either A_V or $A_{H/V}^{\text{adj.}}$ (i.e., with scan-optimized $\alpha_{H/V}$) combined with the $R(K_{\text{DP}}^*)$ retrieval perform better than the $R(Z_h)$ and $R(A_{H/V})$ algorithms, and the $R(Z_h)/R(K_{\text{DP}}^*)$ algorithm shows slightly lower NRMSE values than the $R(A_{H/V}^{\text{adj.}})$-based hybrid estimators when evaluated via rain gauges. Even though α_H is more sensitive to the DSD variability than α_V, the scan-wise adjustments reduce the bias for both $R(A_H^{\text{adj.}})/R(K_{\text{DP}}^*)$ and $R(A_V^{\text{adj.}})/R(K_{\text{DP}}^*)$ and lead to similar retrieval accuracies. Based on the evaluation with independent DSD measurements, the new polarimetry-based QPE products show lower NRMSE and higher CC than the operational gauge-adjusted reflectivity-based RW product, pointing to the availability of near-online products with accuracy. We also showed that $A_{H/V}$-based rainfall retrievals for C band significantly reduce the effects of partial beam blockage compared to all Z_h-based algorithms, even when K_{DP} is used for the higher rain rates. When compared with the algorithms in the existing literature, our $R(Z_h)/R(K_{\text{DP}}^*)$ and $R(A_{H/V}^{\text{adj.}})/R(K_{\text{DP}}^*)$ algorithms show much less errors than the ones based on the DSD measurements of eastern China (Gou and Chen 2021) and Oklahoma (Ryzhkov et al. 2014; Ryzhkov and Zrnić 2019).

Nevertheless, a scan-wise $\alpha_{H/V}$ adjustment did not lead to the expected improvements most probably because of the inhomogeneity of the precipitation regimes within the scan. This remaining inhomogeneity seems to inhibit improvements even more for stratiform cases, because the ever-occurring embedded convection corrupts an adequate Z_{DR}-slope estimate. Finally, we exclude the contribution of intense convective cells from the integration path in the ZPHI method following Wang et al. (2017, 2019) because the employed estimation of A is valid in rain only; a considerably higher and variable $\alpha_{H/V}$ is required for such hot spots (Ryzhkov et al. 2013; Schmidt 2020). However, by ignoring Φ_{DP} within such hotspot and simply connecting

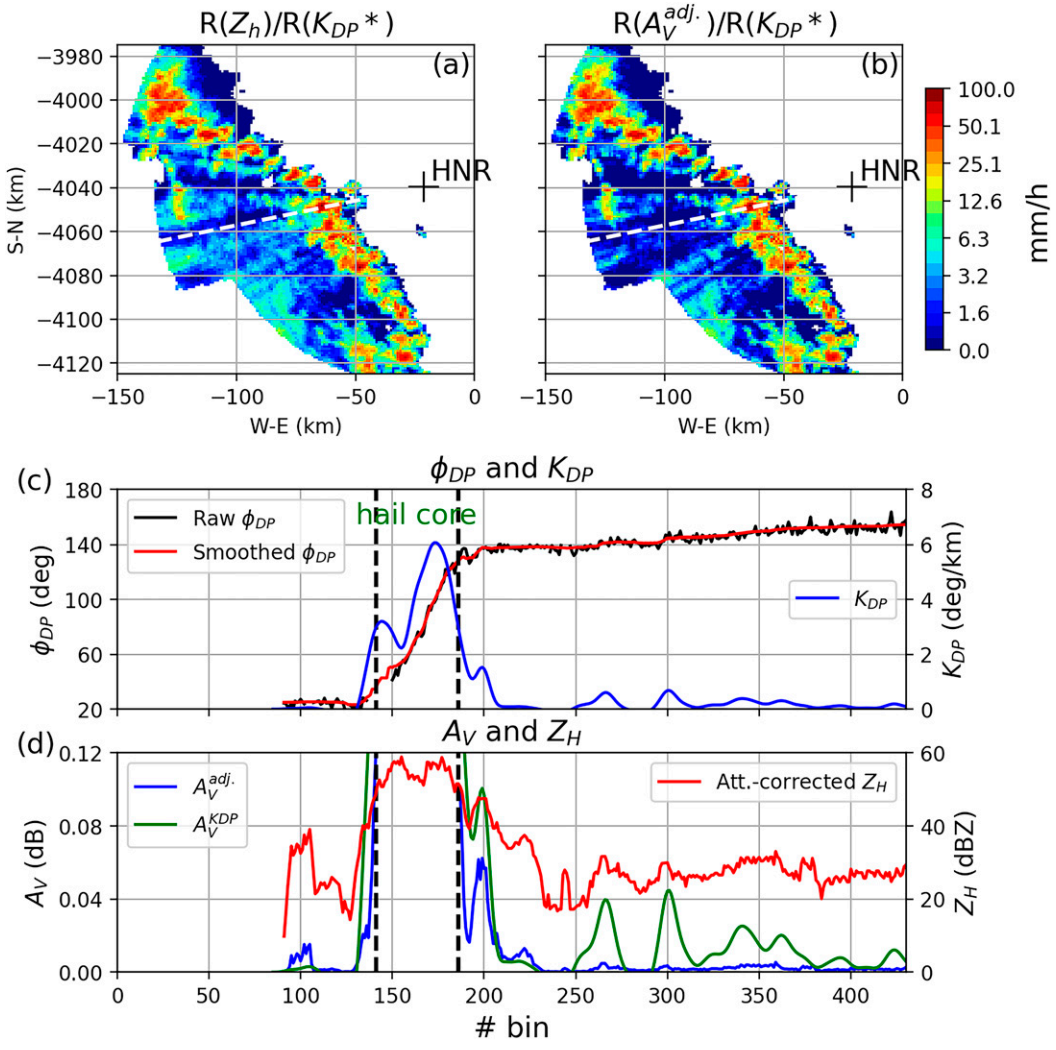

FIG. 11. HNR radar-derived instantaneous rainfall maps of the convective rain event at 1725 UTC 19 Jul 2017 from (a) $R(Z_h)/R(K^*_{DP})$, (b) $R(A_V^{adj.})/R(K^*_{DP})$, and the radial profiles at azimuth 256° of radar variables (c) raw Φ_{DP} in black, smoothed Φ_{DP} in red, and K_{DP} in blue, and (d) attenuation-corrected Z_H in red, $A_V^{adj.}$ in blue, and A_V^{KDP} in green, which is derived from K_{DP} with a scan-wise $\alpha_V = 0.066$ dB per degree ($A_V^{KDP} = \alpha_V K_{DP}$).

pure rain segments into one path will miss the attenuation from the hotspot, which should propagate to the radar bins behind, and lead to underestimated $A_{H/V}$—and thus rainfall—in the latter segment.

In future work, the segmentation of a ray in the case of heavy rain containing large drops or hail, and an optimization of $\alpha_{H/V}$ along the ray are needed to explore the ZPHI procedure in more detail (Huang et al. 2020) and obtain further improvements. More case studies covering a larger variety of rain types need to be analyzed to set up a robust, operational QPE routine exploiting the benefits of $A_{H/V}$ in synergistic use with K_{DP}/K^*_{DP} and Z_h.

Acknowledgments. This work was carried out in the research unit RealPEP (Near-Realtime Quantitative Precipitation Estimation and Prediction, https://www2.meteo.uni-bonn.de/realpep/doku.php), project P1 (Physics-based QPE using polarimetric radars and commercial microwave links), funded by the Deutsche Forschungsgemeinschaft (German Research Foundation) under Grant TR 1023/9-1. We gratefully acknowledge the support of DWD (German Meteorological Service), which provided data used in the study, including Thies disdrometer, C-band dual-polarimetric radar and rain gauge measurements, and the German operational RAdar-OnLine-ANeichung (RADOLAN) rainfall products.

Data availability statement. Rain gauge measurements and the RADOLAN RY and RW rainfall products used in this study are available from the DWD Climate Data Center at https://doi.org/10.5676/DWD_CDC/TRY_BASIS_V001 as cited in Krähenmann et al. (2016). Radar and disdrometer data from DWD are restricted and not publicly available.

REFERENCES

Atlas, D., and C. Ulbrich, 1977: Path- and area-integrated rainfall measurements by microwave attenuation in the 1-3 cm band. *J. Appl. Meteor.*, **16**, 1322–1331, https://doi.org/10.1175/1520-0450(1977)016<1322:PAAIRM>2.0.CO;2.

Battan, L. J., 1973: *Radar Observation of the Atmosphere*. University of Chicago Press, 324 pp.

Beurton, S., and A. H. Thieken, 2009: Seasonality of floods in Germany. *Hydrol. Sci. J.*, **54**, 62–76, https://doi.org/10.1623/hysj.54.1.62.

Bloemink, H. I., and E. Lanzinger, 2005: Precipitation type from the Thies disdrometer. *WMO Tech. Conf. on Meteorological and Environmental Instruments and Methods of Observation*, IOM Rep. 82/WMO/TD 1265, Bucharest, Romania, WMO, 3 pp.

Boodoo, S., D. Hudak, A. Ryzhkov, P. Zhang, N. Donaldson, D. Sills, and J. Reid, 2015: Quantitative precipitation estimation from a C-band dual-polarized radar for the 8 July 2013 flood in Toronto, Canada. *J. Hydrometeor.*, **16**, 2027–2044, https://doi.org/10.1175/JHM-D-15-0003.1.

Brandes, E. A., G. Zhang, and J. Vivekanandan, 2002: Experiments in rainfall estimation with a polarimetric radar in a subtropical environment. *J. Appl. Meteor.*, **41**, 674–685, https://doi.org/10.1175/1520-0450(2002)041<0674:EIREWA>2.0.CO;2.

Bringi, V. N., T. A. Seliga, and W. A. Cooper, 1984: Analysis of aircraft hydrometeor spectra and differential reflectivity (Z_{DR}) radar measurements during the cooperative convective precipitation experiment. *Radio Sci.*, **19**, 157–167, https://doi.org/10.1029/RS019i001p00157.

——, V. Chandrasekar, J. Hubbert, E. Gorgucci, W. L. Randeu, and M. Schoenhuber, 2003: Raindrop size distribution in different climatic regimes from disdrometer and dual-polarized radar analysis. *J. Atmos. Sci.*, **60**, 354–365, https://doi.org/10.1175/1520-0469(2003)060<0354:RSDIDC>2.0.CO;2.

Carey, L. D., and W. A. Petersen, 2015: Sensitivity of C-band polarimetric radar-based drop size estimates to maximum diameter. *J. Appl. Meteor. Climatol.*, **54**, 1352–1371, https://doi.org/10.1175/JAMC-D-14-0079.1.

Clark, R. A., Y. J. Canipe, and D. R. Greene, 1972: Applications of digital radar data in both meteorology and hydrology. *Bull. Amer. Meteor. Soc.*, **53**, 687, https://doi.org/10.1175/1520-0477-53.7.677.

Diederich, M., A. Ryzhkov, C. Simmer, P. Zhang, and S. Trömel, 2015a: Use of specific attenuation for rainfall measurement at X-band radar wavelengths. Part I: Radar calibration and partial beam blockage estimation. *J. Hydrometeor.*, **16**, 487–502, https://doi.org/10.1175/JHM-D-14-0066.1.

——, ——, ——, ——, and ——, 2015b: Use of specific attenuation for rainfall measurement at X-band radar wavelengths. Part II: Rainfall estimates and comparison with rain gauges. *J. Hydrometeor.*, **16**, 503–516, https://doi.org/10.1175/JHM-D-14-0067.1.

Fehlmann, M., M. Rohrer, A. von Lerber, and M. Stoffel, 2020: Automated precipitation monitoring with the Thies disdrometer: Biases and ways for improvement. *Atmos. Meas. Tech.*, **13**, 4683–4698, https://doi.org/10.5194/amt-13-4683-2020.

Gatlin, P. N., M. Thurai, V. N. Bringi, W. Petersen, D. Wolff, A. Tokay, L. Carey, and M. Wingo, 2015: Searching for large raindrops: A global summary of two-dimensional video disdrometer observations. *J. Appl. Meteor. Climatol.*, **54**, 1069–1089, https://doi.org/10.1175/JAMC-D-14-0089.1.

Giangrande, S., S. Collis, A. Theisen, and A. Tokay, 2014: Precipitation estimation from the ARM distributed radar network during the MC3E campaign. *J. Appl. Meteor. Climatol.*, **53**, 2130–2147, https://doi.org/10.1175/JAMC-D-13-0321.1.

Gou, Y., and H. Chen, 2021: Combining radar attenuation and partial beam blockage corrections for improved quantitative application. *J. Hydrometeor.*, **22**, 139–153, https://doi.org/10.1175/JHM-D-20-0121.1.

Huang, H., K. Zhao, H. Chen, D. Hu, P. Fu, Q. Lin, and Z. Yang, 2020: Improved attenuation-based radar precipitation estimation considering the azimuthal variabilities of microphysical properties. *J. Hydrometeor.*, **21**, 1605–1620, https://doi.org/10.1175/JHM-D-19-0265.1.

Hubbert, J., and V. N. Bringi, 1995: An iterative filtering technique for the analysis of copular differential phase and dual-frequency radar measurements. *J. Atmos. Oceanic Technol.*, **12**, 643–648, https://doi.org/10.1175/1520-0426(1995)012<0643:AIFTFT>2.0.CO;2.

Krähenmann, S., A. Walter, S. Brienen, F. Imbery, and A. Matzarakis, 2016: Monthly, daily and hourly grids of 12 commonly used meteorological variables for Germany estimated by the Project TRY Advancement (version v001). DWD Climate Data Center, accessed 16 November 2020, https://doi.org/10.5676/DWD_CDC/TRY_BASIS_V001.

Kurri, M., and A. Huuskonen, 2008: Measurements of the transmission loss of a radome at different rain intensities. *J. Atmos. Oceanic Technol.*, **25**, 1590–1599, https://doi.org/10.1175/2008JTECHA1056.1.

Levenberg, K., 1944: A method for the solution of certain nonlinear problems in least squares. *Q. Appl. Math.*, **2**, 164–168, https://doi.org/10.1090/qam/10666.

Lim, S., R. Cifelli, V. Chandrasekar, and S. Matrosov, 2013: Precipitation classification and quantification using X-band dual-polarization weather radar: Application in the Hydrometeorology Testbed. *J. Atmos. Oceanic Technol.*, **30**, 2108–2120, https://doi.org/10.1175/JTECH-D-12-00123.1.

Matrosov, S., D. Kingsmill, and F. Ralph, 2005: The utility of X-band polarimetric radar for quantitative estimates of rainfall parameters. *J. Hydrometeor.*, **6**, 248–262, https://doi.org/10.1175/JHM424.1.

Nissen, K. M., and U. Ulbrich, 2017: Increasing frequencies and changing characteristics of heavy precipitation events threatening infrastructure in Europe under climate change. *Nat. Hazards Earth Syst. Sci.*, **17**, 1177–1190, https://doi.org/10.5194/nhess-17-1177-2017.

Pejcic, V., P. S. Garfias, K. Mühlbauer, S. Trömel, and C. Simmer, 2020: Comparison between precipitation estimates of ground-based weather radar composites and GPM's DPR rainfall product over Germany. *Meteor. Z.*, **29**, 451–466, https://doi.org/10.1127/metz/2020/1039.

Ryzhkov, A. V., and D. S. Zrnić, 2005: Radar polarimetry at S, C, and X bands comparative analysis and operational implications. *32nd Int. Conf. on Radar Meteorology*, Albuquerque, NM, Amer. Meteor. Soc., 9R.3, https://ams.confex.com/ams/32Rad11Meso/techprogram/paper_95684.htm.

——, and ——, 2019: *Radar Polarimetry for Weather Observations*. Springer, 486 pp.

——, M. R. Kumjian, S. M. Ganson, and P. Zhang, 2013: Polarimetric radar characteristics of melting hail. Part II: Practical implications. *J. Appl. Meteor. Climatol.*, **52**, 2871–2886, https://doi.org/10.1175/JAMC-D-13-074.1.

——, M. Diederich, P. Zhang, and C. Simmer, 2014: Potential utilization of specific attenuation for rainfall estimation, mitigation of partial beam blockage, and radar networking.

J. Atmos. Oceanic Technol., **31**, 599–619, https://doi.org/10.1175/JTECH-D-13-00038.1.

——, P. Zhang, H. Reeves, M. Kumjian, T. Tschallener, S. Trömel, and C. Simmer, 2016: Quasi-vertical profiles—A new way to look at polarimetric radar data. *J. Atmos. Oceanic Technol.*, **33**, 551–562, https://doi.org/10.1175/JTECH-D-15-0020.1.

Scarchilli, G., E. Goroucci, V. Chandrasekar, and T. A. Seliga, 1993: Rainfall estimation using polarimetric techniques at C-band frequencies. *J. Appl. Meteor.*, **32**, 1150–1160, https://doi.org/10.1175/1520-0450(1993)032<1150:REUPTA>2.0.CO;2.

Schmidt, M., 2020: Improvement of hail detection and nowcasting by synergistic combination of information from polarimetric radar, model predictions, and in-situ observations. Ph.D. dissertation, Universität Bonn, 150 pp.

Steinert, J., M. Werner, and P. Tracksdorf, 2013: Hydrometeor classification and quantitative precipitation estimation from quality assured radar data for the DWD C-band weather radar network. *36th Int. Conf. on Radar Meteorology*, Breckenridge, CO, Amer. Meteor. Soc., 363, https://ams.confex.com/ams/36Radar/webprogram/Paper228477.html.

Sun, J., 2005: Initialization and numerical forecasting of a supercell storm observed during STEPS. *Mon. Wea. Rev.*, **133**, 793–813, https://doi.org/10.1175/MWR2887.1.

Testud, J., E. Le Bouar, E. Obligis, and M. Ali-Mehenni, 2000: The rain profiling algorithm applied to polarimetric weather radar. *J. Atmos. Oceanic Technol.*, **17**, 332–356, https://doi.org/10.1175/1520-0426(2000)017<0332:TRPAAT>2.0.CO;2.

——, S. Oury, R. A. Black, P. Amayenc, and X. Dou, 2001: The concept of ''normalized'' distribution to describe raindrop spectra: A tool for cloud physics and cloud remote sensing. *J. Appl. Meteor.*, **40**, 1118–1140, https://doi.org/10.1175/1520-0450(2001)040<1118:TCONDT>2.0.CO;2.

Thompson, E., S. Rutledge, B. Dolan, M. Thurai, and V. Chandrasekar, 2018: Dual-polarization radar rainfall estimation over tropical oceans. *J. Appl. Meteor. Climatol.*, **57**, 755–775, https://doi.org/10.1175/JAMC-D-17-0160.1.

Tokay, A., P. G. Bashor, E. Habib, and T. Kasparis, 2008: Raindrop size distribution measurements in tropical cyclones. *Mon. Wea. Rev.*, **136**, 1669–1685, https://doi.org/10.1175/2007MWR2122.1.

——, W. A. Petersen, P. Gatlin, and M. Wingo, 2013: Comparison of raindrop size distribution measurements by collocated disdrometers. *J. Atmos. Oceanic Technol.*, **30**, 1672–1690, https://doi.org/10.1175/JTECH-D-12-00163.1.

Trömel, S., M. Kumjian, A. Ryzhkov, and C. Simmer, 2013: Backscatter differential phase—Estimation and variability. *J. Appl. Meteor. Climatol.*, **52**, 2529–2548, https://doi.org/10.1175/JAMC-D-13-0124.1.

——, M. Ziegert, A. Ryzhkov, C. Chwala, and C. Simmer, 2014a: Using microwave backhaul links to optimize the performance of algorithms for rainfall estimation and attenuation correction. *J. Atmos. Oceanic Technol.*, **31**, 1748–1760, https://doi.org/10.1175/JTECH-D-14-00016.1.

——, A. V. Ryzhkov, P. Zhang, and C. Simmer, 2014b: Investigations of backscatter differential phase in the melting layer. *J. Appl. Meteor. Climatol.*, **53**, 2344–2359, https://doi.org/10.1175/JAMC-D-14-0050.1.

Vulpiani, G., M. Montopoli, L. Delli Passeri, A. G. Gioia, P. Giordano, and F. S. Marzano, 2012: On the use of dual-polarized C-band radar for operational rainfall retrieval in mountainous areas. *J. Appl. Meteor. Climatol.*, **51**, 405–425, https://doi.org/10.1175/JAMC-D-10-05024.1.

Wang, Y., P. Zhang, A. Ryzhkov, J. Zhang, and P.-L. Chang, 2014: The application of specific attenuation for tropical rainfall estimation in complex terrain. *J. Hydrometeor.*, **15**, 2250–2266, https://doi.org/10.1175/JHM-D-14-0003.1.

——, J. Zhang, P. Zhang, A. V. Ryzhkov, and C. Fritts, 2017: The impact of different precipitation types on the polarimetric radar QPE using specific attenuation. *38th Int. Conf. on Radar Meteorology*, Chicago, IL, Amer. Meteor. Soc., 265, https://ams.confex.com/ams/38RADAR/webprogram/Paper321106.html.

——, S. Cocks, L. Tang, A. Ryzhkov, P. Zhang, J. Zhang, and K. Howard, 2019: A prototype quantitative precipitation estimation algorithm for operational S-Band polarimetric radar utilizing specific attenuation and specific differential phase. Part I: Algorithm description. *J. Hydrometeor.*, **20**, 985–997, https://doi.org/10.1175/JHM-D-18-0071.1.

Waterman, P. C., 1971: Symmetry, unitarity and geometry in electromagnetic scattering. *Phys. Rev. D*, **3**, 825–839, https://doi.org/10.1103/PhysRevD.3.825.

Zacharov, P., and D. Rezacova, 2010: The effect of radar-based QPE on the fractions skill score used at the QPF verification. *Adv. Geosci.*, **25**, 91–95, https://doi.org/10.5194/adgeo-25-91-2010.

Zebisch, M., T. Grothmann, D. Schroeter, C. Hasse, U. Fritsch, and W. Cramer, 2005: Climate change in Germany – Vulnerability and adaptation of climate-sensitive sectors. Klimastatusbericht 2005, Deutscher Wetterdienst, 44–56.

Zhang, J., L. Tang, S. Cocks, P. Zhang, A. Ryzhkov, K. Howard, C. Langston, and B. Kaney, 2020: A dual-polarization radar synthetic QPE for operations. *J. Hydrometeor.*, **21**, 2507–2521, https://doi.org/10.1175/JHM-D-19-0194.1.

Zhang, P., D. Zrnić, and A. Ryzhkov, 2013: Partial beam blockage correction using polarimetric radar measurements. *J. Atmos. Oceanic Technol.*, **30**, 861–872, https://doi.org/10.1175/JTECH-D-12-00075.1.

Zrnić, D. S., and A. V. Ryzhkov, 1999: Polarimetry for weather surveillance radars. *Bull. Amer. Meteor. Soc.*, **80**, 389–406, https://doi.org/10.1175/1520-0477(1999)080<0389:PFWSR>2.0.CO;2.

——, T. D. Keenan, L. D. Carey, and P. May, 2000: Sensitivity analysis of polarimetric variables at a 5-cm wavelength in rain. *J. Appl. Meteor.*, **39**, 1514–1526, https://doi.org/10.1175/1520-0450(2000)039<1514:SAOPVA>2.0.CO;2.